TOF-SIMS analysis of crater residues from Wild 2 cometary on Stardust aluminum foil

Jan LEITNER,[1*] Thomas STEPHAN,[1] Anton T. KEARSLEY,[2] Friedrich HÖRZ,[3] George J. FLYNN,[4] and Scott A. SANDFORD[5]

[1]Institut für Planetologie, Westfälische Wilhelms-Universität Münster, Wilhelm-Klemm-Str. 10, 48149 Münster, Germany
[2]Impact and Astromaterials Research Centre, Department of Mineralogy, The Natural History Museum, London SW7 5BD, UK
[3]NASA Johnson Space Center, Houston, Texas 77058, USA
[4]Department of Physics, SUNY Plattsburgh, Plattsburgh, New York 12901, USA
[5]Astrophysics Branch, NASA-Ames Research Center, Moffett Field, California 94035, USA
[*]Corresponding author. E-mail: leitner@ uni-muenster.de

(submitted to Meteoritics & Planetary Science; December XX, 2006)

Abstract–Impact residues of cometary particles on aluminum foils from the Stardust mission were investigated with TOF-SIMS for their elemental and organic composition. The residual matter from comet 81P/Wild 2 shows a wide compositional range, from nearly monomineralic grains to polymict aggregates. Despite the comparably small analyzed sample volume, the average element composition of the investigated residues is similar to bulk CI chondritic values. Analysis of organic components in impact residues is complicated, due to fragmentation and alteration of the compounds during the impact process and by the presence of contaminants on the aluminum foils. Nevertheless, polycyclic aromatic hydrocarbons (PAHs) that are unambiguously associated with the impact residues were observed, and thus are most likely of cometary origin.

INTRODUCTION

In January 2006, the Stardust mission returned cometary matter to Earth that was collected during its passage through the coma of comet 81P/Wild 2 in January of 2004 (Brownlee et al. 2003; Tsou et al. 2003). These samples offer the first opportunity to analyze cometary matter collected under controlled conditions. During the cruise phase, before the cometary encounter, Stardust also collected contemporary interstellar dust on the rear side of the collector tray.

Stardust used two different types of capture media for both cometary and interstellar dust. Low-density, SiO_2-based aerogel was used as the primary medium to gently decelerate the impinging particles more or less intact (Tsou et al. 2003). In contrast, on the second capture medium, aluminum foil (Al 1100; >99 % pure), particles came to an abrupt stop and produced hypervelocity craters. These foils were mainly used to facilitate the removal of the aerogel tiles from the modular collector trays following return to Earth (Tsou et al. 2003). However, Al foil exposed to the comet also provided a valuable capture medium, since impactor residues were found, typically as discontinuous layers of shock-produced melts, inside crater cavities or on crater rims.

In the present study, residual cometary matter in craters on the Stardust Al foils was analyzed by time-of-flight secondary ion mass spectrometry (TOF-SIMS) in order to determine the elemental and organic composition of the dust and thereby properties of the cometary nucleus itself. Earlier investigations (Stephan et al. 2005; Hoppe et al. 2006; Leitner

et al. 2006a; 2006b) on experimental craters have shown that from the elemental composition of the residual matter in craters, the projectile material can be identified and its composition can be revealed *cum grano salis*, despite the significant, shock-induced alterations at the Stardust encounter speed of 6.12 km/s, even for small grains.

SAMPLES AND EXPERIMENTAL METHODS

A total of eight foils from the cometary side of the *Sample Tray Assembly* (STA) of the Stardust spacecraft was selected for TOF-SIMS analysis. These foils are C2009N,1, C2026N,1, C2029W,1, C2070W,1, C2086N,1, C2086W,1, C2091N,1, and C2101W,1. Only foils C2009N,1, C2029W,1, C2086N,1, C2086W,1, C2091N,1, and C2102N,1 contained craters with diameters >10 µm, illustrated in Fig. 1.

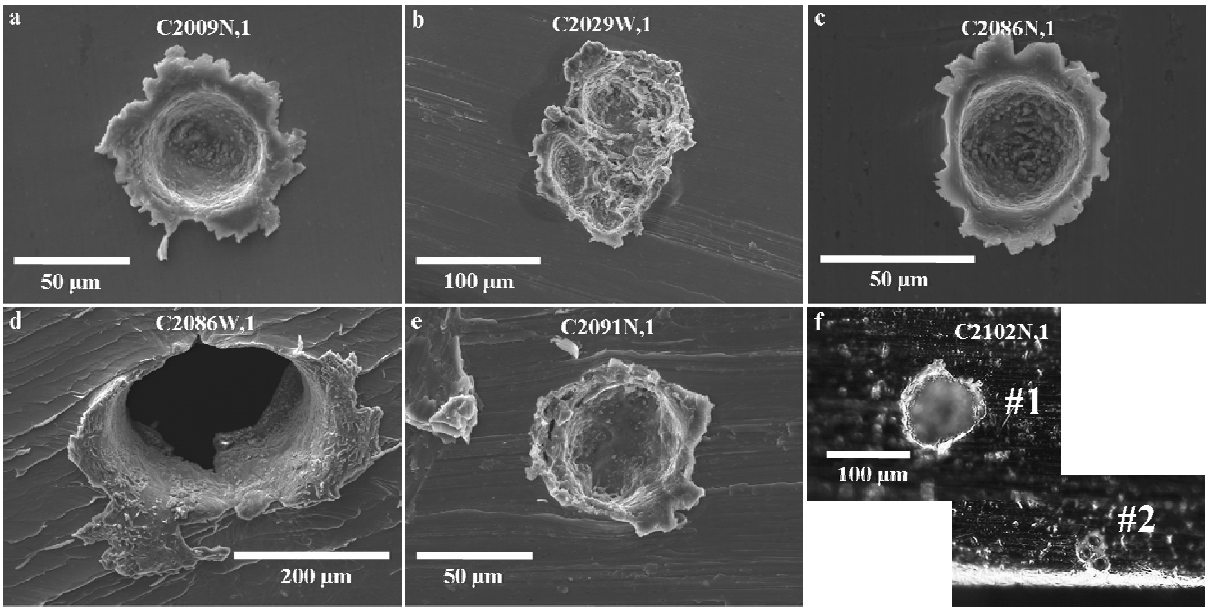

Fig. 1. Secondary electron (a–e) and optical microscope (f) images of Stardust craters on Al foil investigated in this study. For C2102N,1, no secondary electron images were available.

Since these foils were not perfectly flat after cutting and removal from the STA by NASA's Curatorial Staff, they had to be flattened prior to detailed analyses. This was achieved by slightly stretching the foils by ~2.5 %, which was carried out by F. J. Stadermann at Washington University, St. Louis, Missouri. After straightening, the samples were analyzed using a TOF-SIMS IV instrument from ION-TOF equipped with a gallium liquid metal ion source for SIMS analysis and an argon ion source for sputter cleaning. TOF-SIMS usually requires flat surfaces. Obviously Al foil craters, even after flattening of the foils, are not perfectly flat. The remaining surface topography slightly degraded the mass resolution $(m/\Delta m)_{FWHM}$ from ~5500 to ~4000 at mass 29 u. Further topographic effects are well understood and have been described in the literature (Rost et al. 1999). However, one has to keep in mind that the primary ion beam reaches the sample under 45° and, therefore, not all sample regions in the crater or on the crater rim can be accessed by the ion beam in any single measurement. Therefore, selected craters were analyzed twice, in different orientations, to provide access to a larger portion of the residues in these craters.

In order to remove an omnipresent, thin contamination layer, the sample surfaces had to be cleaned by Ar^+ ion bombardment prior to measurement. To ensure proper cleaning of the non-

flat craters, the sample was rotated four times by 90° during this procedure. On the other hand, complex molecular ions like, e.g., PAHs are destroyed during this process, the reason why TOF-SIMS measurements were carried out before and after sputter cleaning.

During the analyses, individual sample areas were rastered (128^2, 256^2, or 512^2 pixels) with a ~0.2 µm $^{69}Ga^+$ primary ion beam with a repetition rate of 10 kHz and a pulse width of ~1.5 ns.

Based on the lateral distributions of secondary ions of the major elements, as judged from qualitative elemental maps, regions of interest were selected for the generation of quantitative mass spectra and determination of element ratios using relative SIMS sensitivity factors derived from glass standards. All abundances presented here are atomic element ratios relative to Si and, in some cases, normalized to CI chondritic composition. Further details are given in the literature (Stephan 2001; Hoppe et al. 2006).

Because the impinging cometary dust particles and their melts have incorporated variable amounts of foil material, the elemental composition of the crater residues obtained from the analyses does not resemble exactly the original composition of the impactors. Thus, a data correction using elemental ratios from the surrounding aluminum blank was applied as described by Hoppe et al. (2006).

Blank correction

After selecting a region of interest containing the residual projectile matter, the fraction of silicon that belongs to the cometary particle Si_r/Si has to be determined, since silicon is used as reference element throughout this study. Si_r stands for the silicon belonging to the residue, while Si without index denotes the silicon measured during analysis. With Si_b, the silicon belonging to the foil blank, we have

$$Si = Si_r + Si_b \,. \tag{1}$$

Similarly,

$$Al = Al_r + Al_b \,. \tag{2}$$

The latter term can now be transformed into

$$Al = \frac{Si_r Al_r}{Si_r} + \frac{Si_b Al_b}{Si_b} \tag{3}$$

With

$$\begin{aligned} \frac{Al}{Si} &= \frac{Si_r Al_r}{SiSi_r} + \frac{Si_b Al_b}{SiSi_b} \\ &= \frac{Si_r Al_r}{SiSi_r} + \frac{(Si - Si_r) Al_b}{SiSi_b} \\ &= \frac{Si_r Al_r}{SiSi_r} + \frac{SiAl_b}{SiSi_b} - \frac{Si_r Al_b}{SiSi_b} \\ &= \frac{Si_r}{Si}\frac{Al_r}{Si_r} + \frac{Al_b}{Si_b} - \frac{Si_r}{Si}\frac{Al_b}{Si_b} \end{aligned} \tag{4}$$

it follows that

$$\frac{Al}{Si} - \frac{Al_b}{Si_b} = \frac{Si_r}{Si}\left(\frac{Al_r}{Si_r} - \frac{Al_b}{Si_b}\right) \tag{5}$$

and finally

$$\frac{Si_r}{Si} = \frac{\frac{Al}{Si} - \left(\frac{Al}{Si}\right)_b}{\left(\frac{Al}{Si}\right)_r - \left(\frac{Al}{Si}\right)_b}. \tag{6}$$

Equations 1 and 2 can be generalized for any given element E that consists of a fraction that stems from the impactor and another one that is inherent in the foil blank,

$$E = E_r + E_b. \tag{7}$$

Since we are interested in the silicon-normalized abundance, we search for $(E/Si)_r$. This term can be written as

$$\frac{E_r}{Si_r} = \frac{E}{Si_r} - \frac{E_b}{Si_r} \tag{8}$$

and then transformed into

$$\begin{aligned} \frac{E_r}{Si_r} &= \frac{(E/Si)}{(Si_r/Si)} - \frac{E_b}{Si_b}\frac{Si_b}{Si_r} \\ &= \frac{(E/Si)}{(Si_r/Si)} - \frac{E_b}{Si_b}\left(\frac{Si}{Si_r} - \frac{Si_r}{Si_r}\right) \end{aligned} \tag{9}$$

and finally

$$\left(\frac{E}{Si}\right)_r = \frac{(E/Si)}{(Si_r/Si)} - \left(\frac{E}{Si}\right)_b\left(\frac{1}{Si_r/Si} - 1\right). \tag{10}$$

With Equation 10, $(E/Si)_r$ can be derived from measured quantities using Si_r/Si from Equation 6. Since the initial composition of a captured cometary particle is unknown, we assume further that the sample has a CI-like Al/Si-ratio. Consequently Equation 6 becomes

$$\frac{Si_r}{Si} = \frac{\frac{Al}{Si} - \left(\frac{Al}{Si}\right)_b}{\left(\frac{Al}{Si}\right)_{CI} - \left(\frac{Al}{Si}\right)_b}. \tag{11}$$

Certainly, the use of CI chondritic Al/Si-ratios is only a first-order approximation. However, for all investigated sample areas, >96 % of the analyzed material stems from the foil blank. Therefore, an uncertainty in the indigenous Al/Si-ratio has only a minor effect on the determined element ratios and the CI approximation is certainly valuable. Even with the assumption that there was no indigenous Al at all in the cometary particles, the corrected data differ less than 7 % from the CI-corrected values.

The order of magnitude of these corrections varies from nearly zero to about 100 % of the uncorrected abundances, since different foils and even different areas of the same foil show large variations in their local elemental composition. Therefore, all data were discarded wherever the blank signal was found to be higher than 50 % of the entire signal or where the lateral distribution of the contamination was obviously heterogeneous, and therefore a clear attribution of the measured signal to cometary material could not be made.

Analysis of standards

Prior to analyzing the Wild 2 samples, several standards of well-known compositions, were shot at 4.2–6.1 km/s into aluminum foil and investigated by TOF-SIMS (Stephan et al. 2005; Hoppe et al. 2006; Leitner et al. 2006a; 2006b) in order to evaluate the reproducibility of the chemical composition of the projectile materials by TOF-SIMS analysis. These standards included powders from the CV chondrite Allende, as reported earlier (Stephan et al. 2005; Hoppe et al. 2006), and were extended in this study, using the light gas gun at University of Kent, to hornblende (USNM 143965), diopside (Yates Mine), olivine (Admire), bytownite, and pyrrhotite. Anton, could you add a few words and/or a reference?

The blank correction for the mineral standards was calculated as described above. Therefore, Al/Si-ratios obtained from reference data like EDS-analyses were used instead of a CI-like Al/Si-ratio.

RESULTS

Mineral standards

Quantitative results obtained from mineral standards are summarized in **Error! Reference source not found.**. All single-mineral standards could be identified unambiguously from the TOF-SIMS analysis of their crater residues. In comparison to their element ratios from literature data or SEM-EDX data (REFERENCE: Kearsley et al.?), correlation coefficients >0.99 were found.

These reference measurements suggest that there are no major modifications of the impactor composition during the impact process at velocities up to 6.1 km/s, at least for the major elements. The largest deviations from the nominal values occur only for some minor constituents of the minerals with abundances of less than 1 wt%. Na and K in the investigated hornblende standard are <1 wt%, the diopside contains <0.5 wt% Na, while the olivine contains 0.011±0.005 wt% Ca. These elements may be affected by mobilization effects. In a previous study, modest to significant loss of Na and K, in combination with an increase in refractory elements, especially Ca, in the impact melts was observed (Hörz et al. 1983).

This was reported for the main fraction of the residue inside the impact craters. The increased alkali abundances in the residue on the crater lips (**Error! Reference source not found.**), the areas accessible for TOF-SIMS analysis, possibly are the result of recondensation of mobilized volatiles on the crater rim. However, for the the bytownite mineral standard with ~2 wt% Na, no deviation between EDX and TOF-SIMS data was observed. Therefore, it seems to be plausible that the mobilization and recondensation processes affect only volatiles that occur only in traces and not elements that are part of the mineral structure.

.Furthermore, Na, K and Ca may be influenced by contamination present on the foils. **Error! Reference source not found.** shows examples from three craters for such heterogeneously distributed elements in the Al foil blank. For all craters, significant abundances of the displayed ion species are present in the vicinity of each crater.

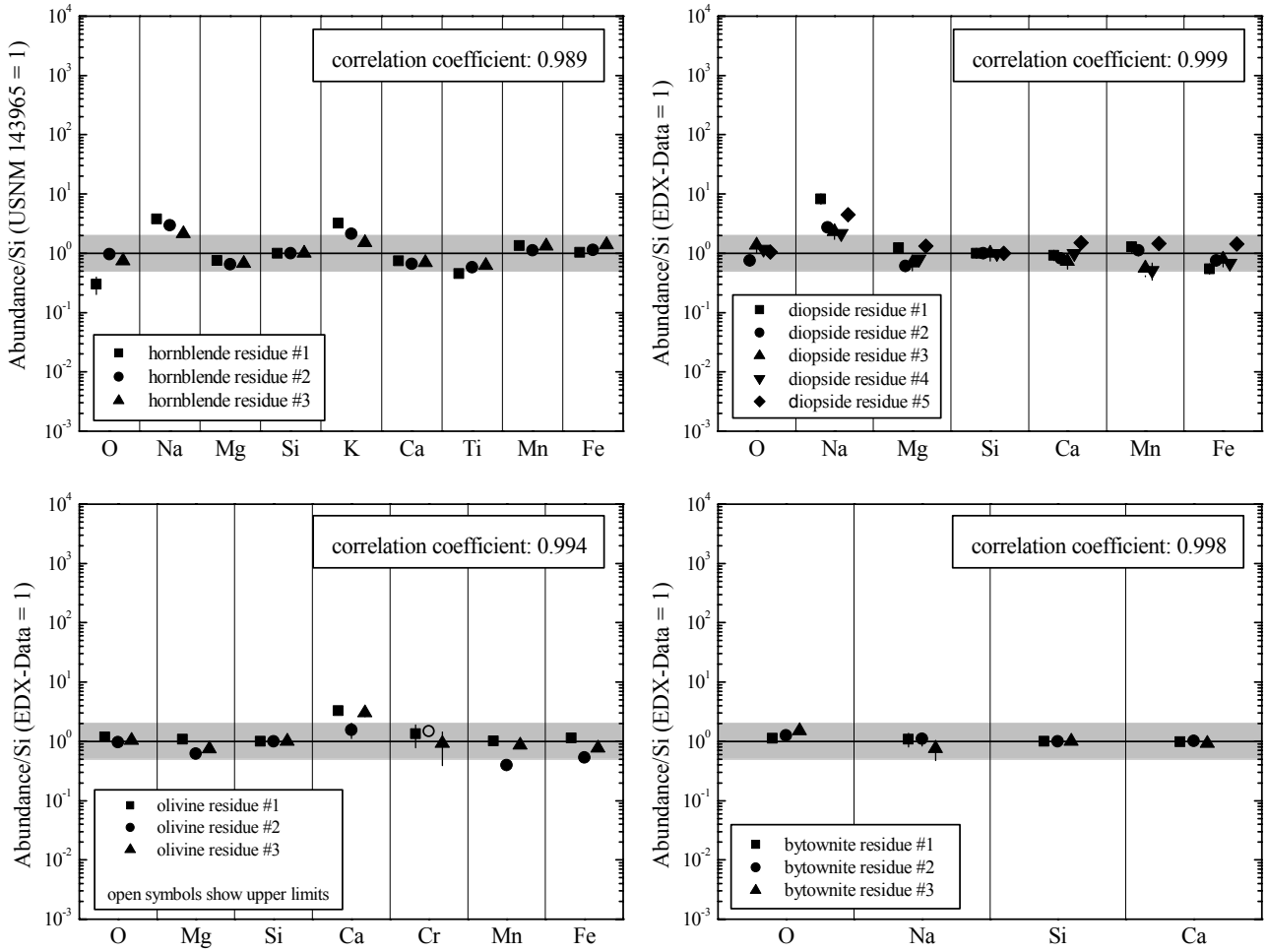

Fig. 2. Element abundances relative to Si and normalized to literature values or SEM-EDX analytical results for mineral standards. The gray bars mark the range between 0.5 and 2 times the reference values.

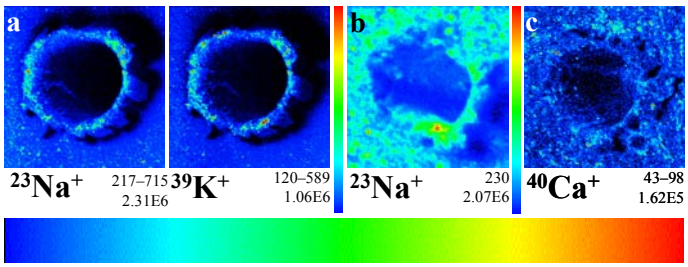

Fig. 3. Secondary ion images of crater residues of several mineral standards. The ion species is mentioned below each image. Also below each image are the maximum intensity per pixel or an intensity range, to which the ion image is normalized, and the integrated intensity of the whole image. The color bar represents a linear scale from black (zero intensity) to red (maximum intensity). All subsequent secondary ion images are displayed in this way. (a) Crater from a hornblende projectile, field of view 350×350 µm^2. (b) Crater produced by a diopside projectile, field of view 43.5×43.5 µm^2. (c) Olivine crater residue, field of view 103×103 µm^2.

Foils without large craters – C2026N,1, C2070W,1, and C2101W,1

No craters with diameters >10 µm were found on these foils. Instead, different features were observed, including depressions and scratches in the Al foils, deposits on the foil surfaces as well as impurities inherent to the Al foils.
Secondary ion images are displayed in Figs. 4–6.

Fig. 4a and b show two examples of features observed on foil C2026N,1. In

Fig. 4a, a Si- and Ca-rich feature is visible. The low intensity of Al^+ in this region indicates that the Si- and Ca-bearing structure is a particle located on the foil surface covering the Al foil. Furthermore, a second hotspot containing Mg and Si is also visible in

Fig. 4a..
The SI images in

Fig. 4b show another hotspot on the same foil. It contains Na, Mg, Si, K, Ca, Fe, and Tl. The identification of Tl was unambiguous, since both isotopes with masses of 203 u and 205 u were present, and the measured ratio of $^{205}Tl/^{203}Tl = 2.3 \pm 0.1$ is within error limits identical to the terrestrial value of 2.39.

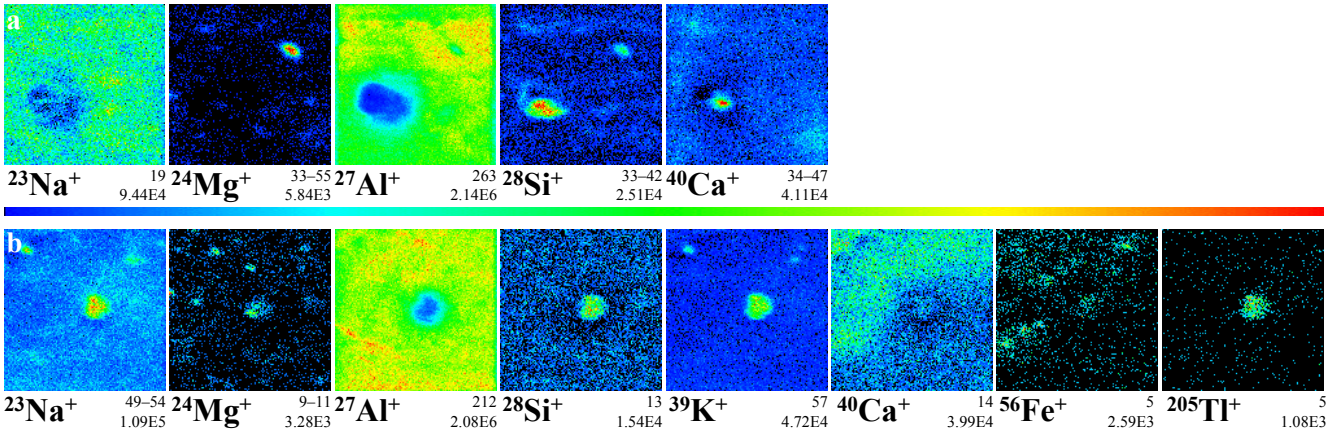

Fig. 4. Secondary ion images of different contamination features, not correlated to impact craters, found on foil C2026N,1. (a) Field of view 13.4×13.4 µm^2, (b) field of view 15.2×15.2 µm^2.

In Fig. 5a–f, several features located on foil C2070W,1 are displayed. Figures a, b, and c show examples for material that was identified by its composition most likely as aerogel debris, since its main constituents besides Si are hydrocarbons. In Fig. 5d, scattered hotspots of several elements can be seen. Correlations exist for Mg and Ti as well as for Ni and Cu, respectively.

Fig. 5e and f show secondary ion images of two regions on foil C2070W,1 with correlated Mg and Si hotspots. Although Na, K, Ca, and Ti have a similar lateral distributions in the area shown in Fig. 5e, there is no correlation of these elements with Mg and Si. For Fig. 5f instead, especially Ti, but also Na, K, and Ca are distributed quite similar to Mg and Si.

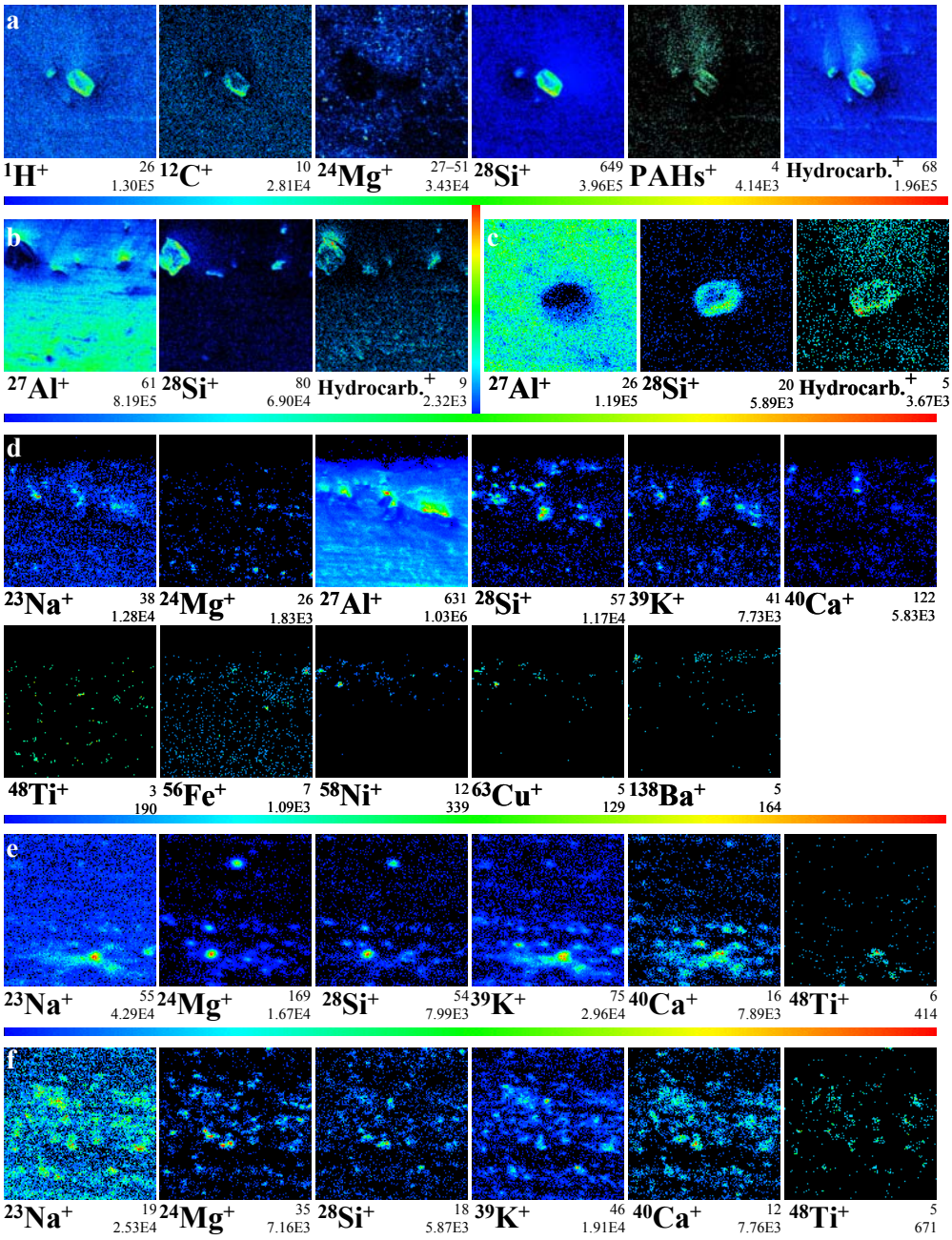

Fig. 5. Features (presumed contaminants) found on C2070W,1. (a) Field of view 78.8×78.8 µm^2, (b) field of view 18.7×18.7 µm^2, (c) field of view 101×101 µm^2, (d) field of view 25.2×25.2 µm^2, (e) field of view 30.8×30.8 µm^2, (f) field of view 30.8×30.8 µm^2.

In

Fig. 6, some examples of the Si-rich contaminations on foil C2101W,1 can be seen. While the figures a, c, and d, show typical element distributions for aerogel debris, i.e. the areas of low Al abundance correlate with high Si intensities, figure b shows a different distribution. The spot in the center of the Al secondary ion image with nearly no signal intensity seems to be a ‘dent’ in the foil with a Si-filled scratch at its upper left corner, since no other SI species was detected in this area, except for three Ti-spots.

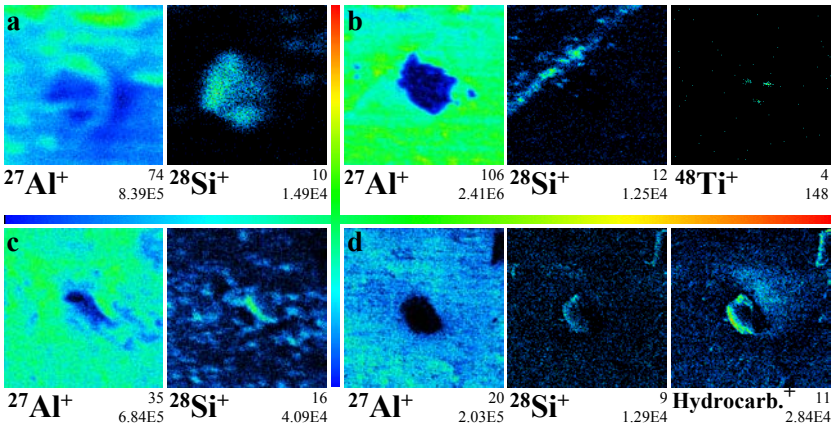

Fig. 6. Features (presumed contaminants) found on C2101W,1. (a) Field of view 9.7×9.7 μm^2, (b) field of view 24.8×24.8 μm^2, (c) field of view 25.3×25.3 μm^2, (d) field of view 100×100 μm^2..

Fig. 7 shows the abundances of several elements relative to Si for six individual Mg- and Si-rich spots, of which three are displayed in Fig. 4a,Fig. 5e and Fig. 5f. Besides Si and Mg, the main constituents are C and O, while other elements contribute only very little to the composition.

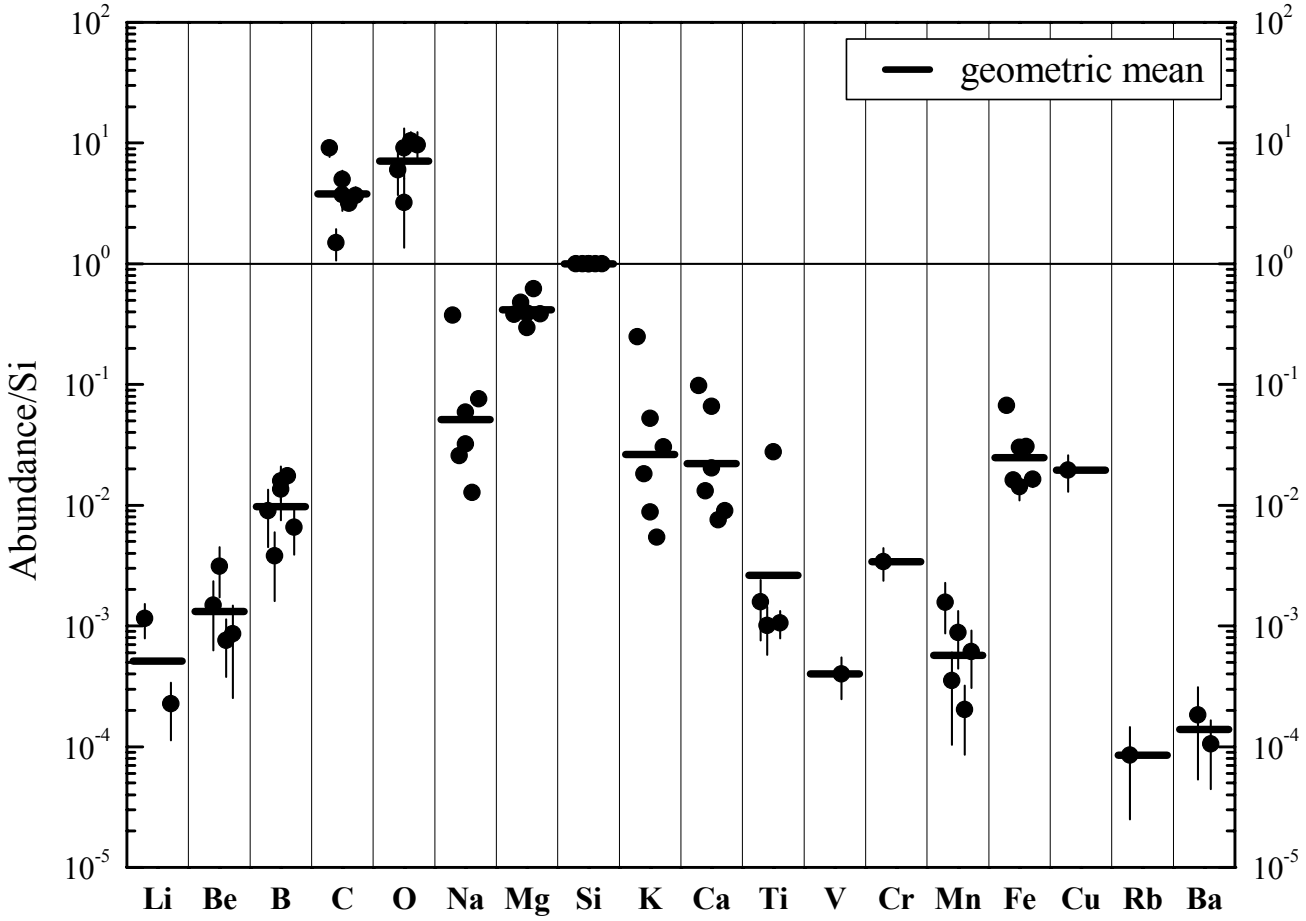

Fig. 7. Elemental abundances normalized to Si of Mg- and Si- rich features found on foils C2026N,1 and C2070W,1.

Fig. 8 shows the element abundances relative to Si for five features whose compositions are dominated by Si, C, and O, and which also contain abundant hydrocarbons, as can be seen in

Fig. 4b, Fig. 5a , b, c, and Fig. 6d.

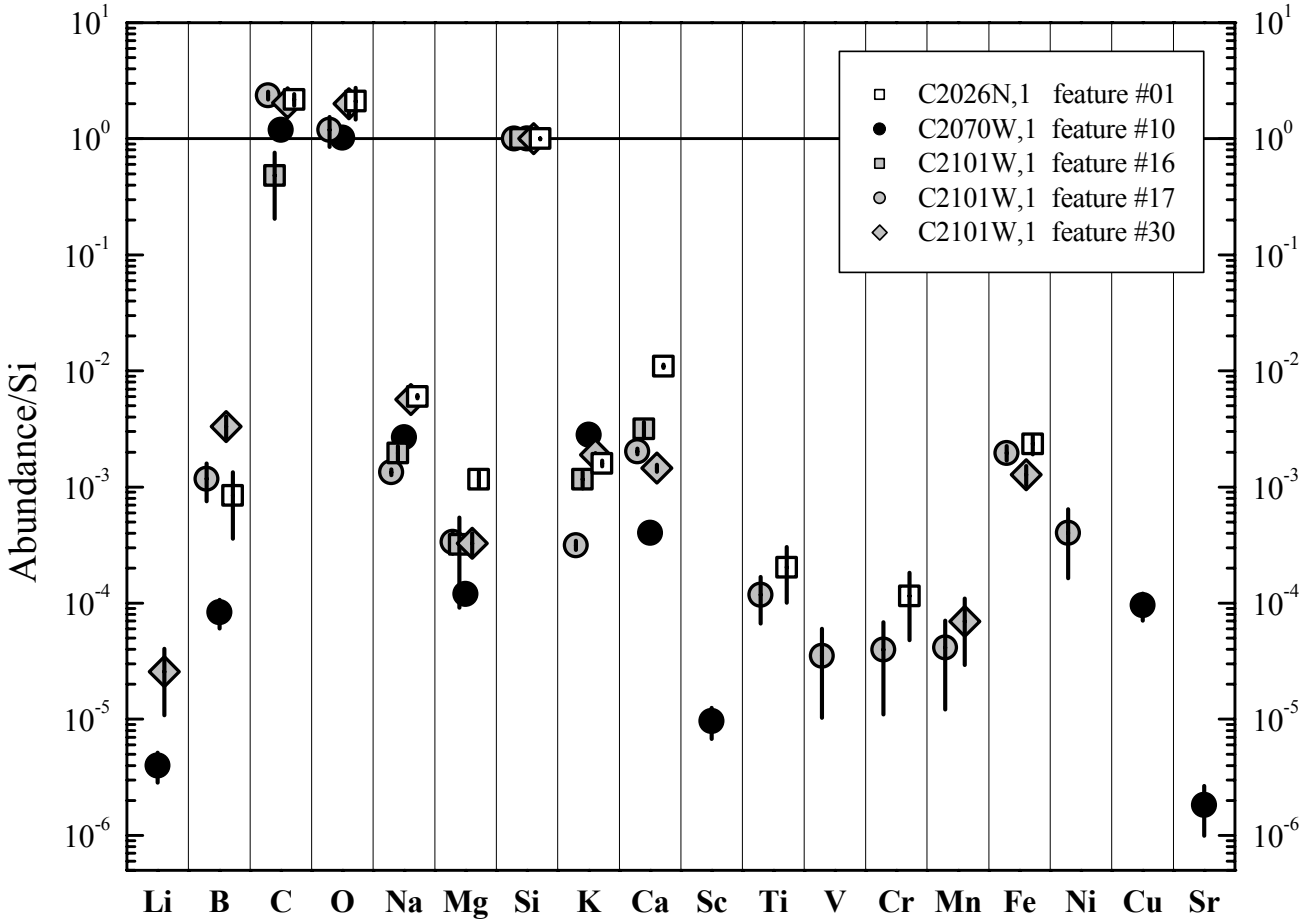

Fig. 8. Elemental abundances relative to Si are shown for five Si-rich features (probably aerogel debris).

Large foil craters

On six of the investigated foils, seven large impact craters between 50 and 240 µm in diameter were found and their residues were analyzed with TOF-SIMS. Quantitative results are summarized in Fig. 16 as element ratios relative to Si and normalized to CI ratios. Since only polymict crater residues are expected to comply with CI chondrite bulk composition, element abundances of monomineralic particles or impactors consisting of distinct mineral mixtures should substantially deviate from the CI abundance pattern. Element ratios relative to Si without CI-normalization are comprised in Table 1.

C2009N,1

On this foil, one crater with a diameter of ~64 µm was found. Here, residual matter within the crater rim was unambiguously identified (Fig. 9). No considerable element abundances were visible outside the crater. Element distribution in the residue on the crater rim is quite heterogeneous, so local hot spots for virtually all major constituents can be seen in the secondary ion images (Fig. 9). The lateral distributions of C, Na, Cl, K, Ti, Ni, and Cu are correlated, as well as the distributions of Mg, Si, S, Cr, Mn, and Fe. Ca was not found above background in this residue.

The area of the crater rim rich in Ni and Cu shows virtually no correlation with other metal distributions, especially not with Fe. Ni and Cu show elemental ratios that are much higher than observed in CI chondrites: Ni/Si is ~26×CI, Cu/Si even higher, ~840×CI.

Most of the major elements in this residue are within a factor of 2 CI chondritic ; only Li and K have slightly higher abundances compared to CI together with modest depletions in Fe and Co..

The absence of Ca and the (Mg+Fe)/Si-ratio of ~1 (cf. Table 1) suggest a pyroxene-dominated composition of this cometary particle.

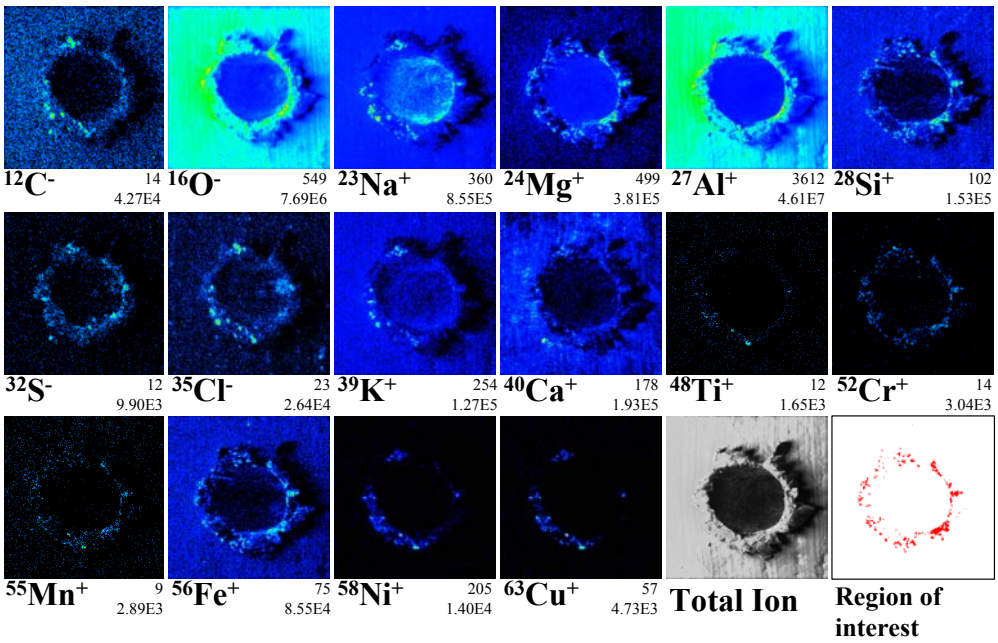

Fig. 9. Secondary ion images of the large crater on foil C2009N,1. In addition to the secondary ion images of the different ion species, a grayscale total positive secondary ion image is displayed, followed by the region of interest that was selected for the quantitative analysis of the residue. The field of view is 120×120 µm^2.

C2029W,1

The large crater, measuring approximately ~160 µm×120 µm in size, on this foil has an irregular shape. It is most likely the result of an aggregate impact, since several circular sub-areas are discernible in Fig. 1b and Fig. 10. Because of the rough topography of the sample area, only a part of the residue was initially accessible for TOF-SIMS investigation. Therefore, the sample was rotated by 180° following the first measurement and analyzed again (Fig. 10b). In the second analysis, some areas that were not accessible during the first investigation were reached by the primary ion beam.

In Fig. 10a and b, C-rich spots in the rim area are visible. These spots are not directly connected with any other major constituents of the residue, but seem to be located in regions devoid of other atomic species.

Residue material is visible on the right side of the crater (Fig. 10a), containing O, Na, Mg, Si, S, K, Ca, Fe, and Ni. Si abundance in this residue is very low, so the inferred element ratios displayed in Fig. 16 show large deviations from CI. Na and Mg show high abundances relative to Si (Table 1), while Fe is in the same order of magnitude as Si and correlates laterally with S in the residue(Fig. 10).

After rotating the sample, another patch of residue was visible on the right side of the crater (Fig. 10b). Also, the residual matter of this patch contains only very little Si, while O, Na, Mg, S, K, Ca, and Fe are comparable to the residue analyzed before sample rotation.

The comparably low abundance of Si in the residual matter indicates that the aggregate particle generating this crater has no silicate composition. Furthermore, the well-correlated lateral distributions of S and Fe suggest that part of the impactor consisted of FeS, even when the S-abundance cannot be quantified by TOF-SIMS, since no sensitivity factors exist due to a lack of suitable standard materials.

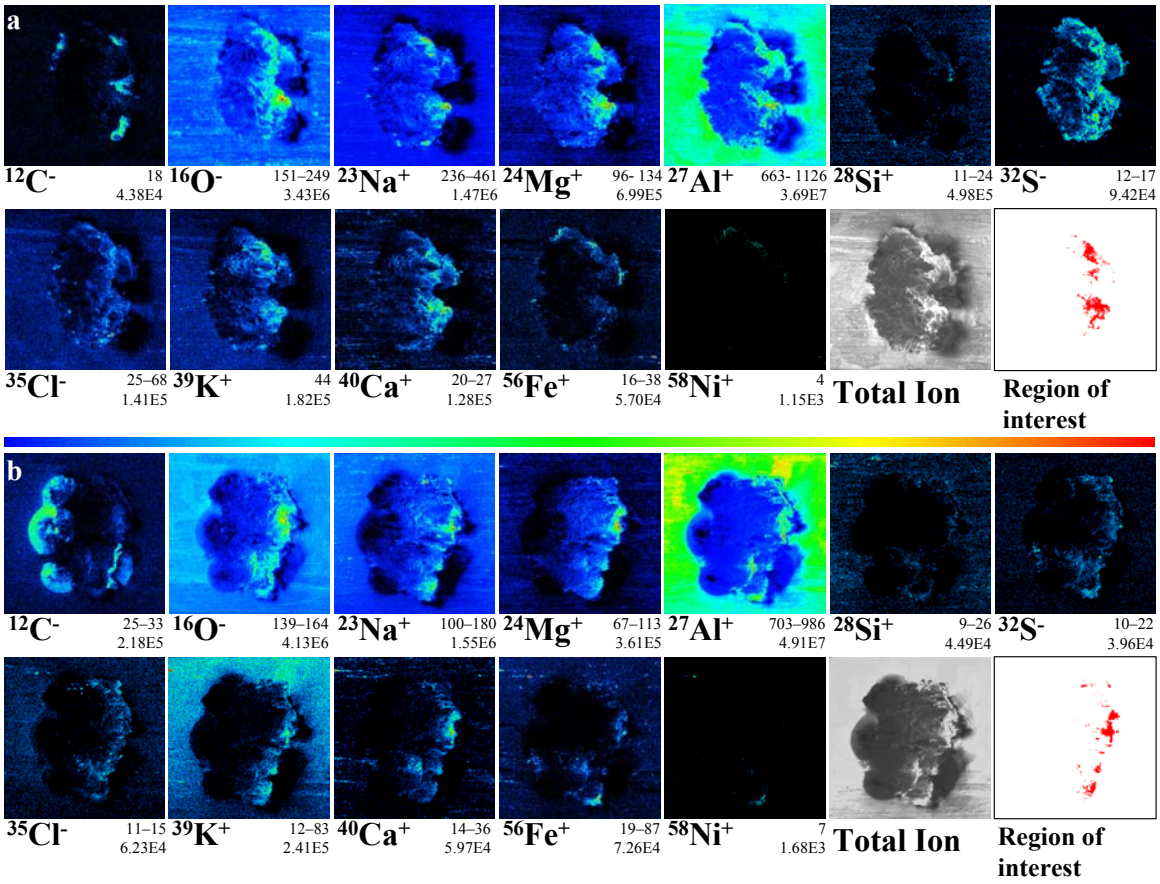

Fig. 10. Secondary ion images of a large crater on foil C2029W,1. (a) Before sample rotation, (b) after sample rotation (180° relative to the orientation in Fig. a). For both figures, the field of view is 199×199 µm^2.

C2086N,1

A crater with a diameter of ~59 µm was found in this foil. Residual matter was concentrated in the upper right quadrant of the impact crater, containing abundant O, Na, Mg, Si, S, Cl, K, Ti, Cr, Mn, and Fe, while virtually no Ca was found (Fig. 11 and Table 1).

Abundances of almost all elements (Fig. 16) are near bulk CI values, only Mn and Fe are depleted by factors of 10 and 30, respectively. Ca was not found in the residue. This composition indicates that the particle is dominated by Mg-rich minerals like enstatite and forsterite, since the Mg/Si-ratio is ~1.2 (Table 1). However, a monomineralic nature of the cometary particle cannot be confirmed, since the great similarity of most element ratios with CI chondritic composition indicates a mixture of different components.

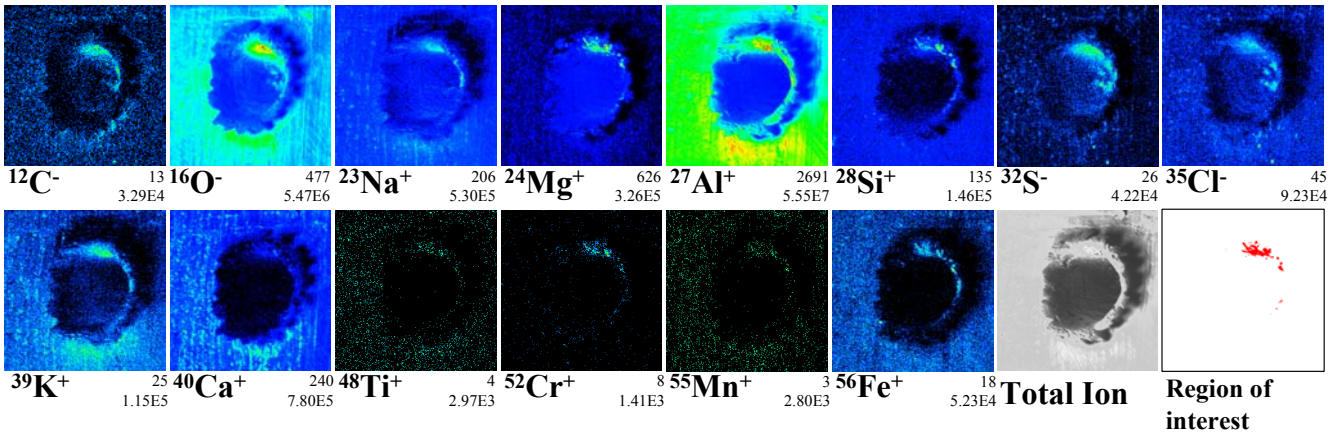

Fig. 11. Secondary ion images of the large crater located on foil C2086N,1. The field of view is 100×100 μm^2.

C2086W,1

This foil contained one crater with a diameter of ~240 μm; the projectile was large enough to completely penetrate the foil. From the secondary ion images, residual material in the "southwestern" and "southern" region of the crater can be recognized. The compositional heterogeneity of the surrounding Al foil is especially evident in the distributions of Si, K, Ca, Ti, and Mn (Fig. 12a and b). The large patch of residue in the lower right quadrant contains amounts of C, O, Na, Mg, Si, Ca, Sc, Mn, and Fe, while the spot in the "south" consists of O, Mg, Si, S, Cl, Ca, Sc, Mn, and Fe. This spot is the location where Stadermann et al. (2006) reported a presolar grain.

Because of the size of the crater, a second analysis was performed after rotating the sample for 180° to investigate parts of the crater rim that were not accessible during the first measurement. While the region containing the residual material that was located in the "southwest" before rotating the crater is not visible any more, in the "northeast", a second patch of residue becomes visible after rotation. The cometary material contains abundant C, O, Na, Mg, Si, S, Cl, K, Ca, and Fe as well as traces of Ti and Mn.

Na abundance is considerably high in all residual patches, as well as K in the residue accessible after sample rotation. Li, Ca, Sc, Ti and Mn show concentrations relative to Si well within a factor of 2 of bulk CI composition. Mg and Fe, however, are slightly depleted in all residues showing relative abundances of ~0.4×CI, while Ni is even lower with ~0.2×CI.

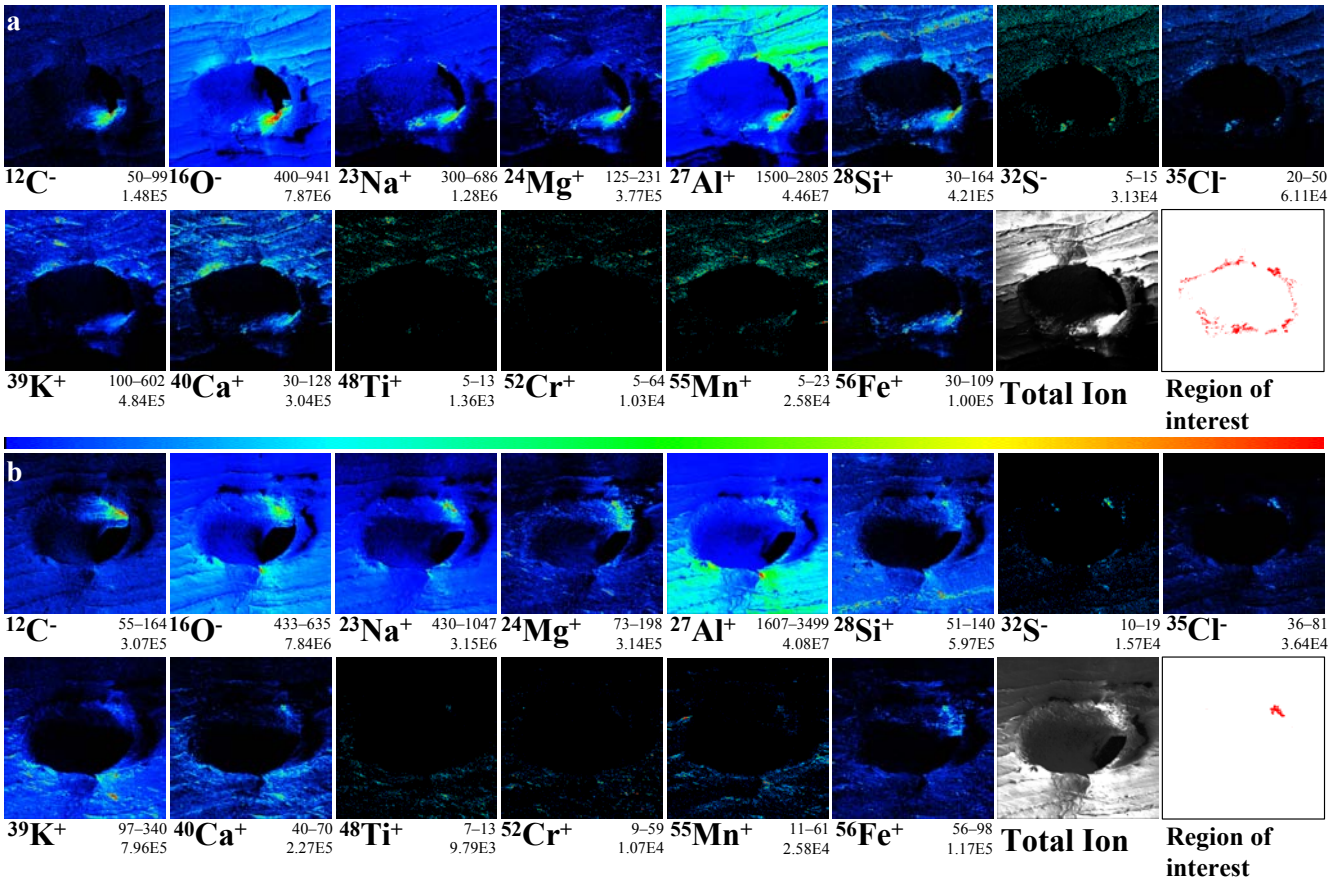

Fig. 12. Secondary ion images of the large penetration crater found on foil C2086W,1. (a) Before sample rotation, (b) after sample rotation (180° relative to the orientation in Fig. a). For both figures, the field of view is 500×500 µm^2.

C2091N,1

The large crater on this foil has a diameter of ~60 µm and unambiguously identifiable residual material at the right side of the crater rim (Fig. 13). The foil area in the vicinity of the crater shows high abundances of Si, K, Ca, Cr, Mn, and Fe, all heterogeneously distributed. The residue is rich in Na, Mg, and Si and has a considerable amount of Fe (Table 1**Error! Reference source not found.**) and S. Furthermore, traces of Li, K, Sc, Cr, Co and Ni are found, while Ca and Ti have no clear connection to the crater rim. This is also the case for Mn; though a reasonably high signal intensity (Fig. 13) is detected in the rim area. However, the Mn-abundance in surrounding foil areas denies a clear connection of Mn with the residue after blank correction.

For this residue, too, the Na abundance is relatively high (Fig. 16, **Error! Reference source not found.**). Li, Mg, K, Sc, and Cr values are all well within 2–3×CI. Fe, Co, and Ni abundances relative to Si are factors of 2–10 lower than in CI carbonaceous chondrites.

The composition of this residue is similar to the one of C2009N,1, so the same assumption may be made for this cometary particle, i.e., a considerable part of the impactor may have a pyroxene- or olivine-like structure.

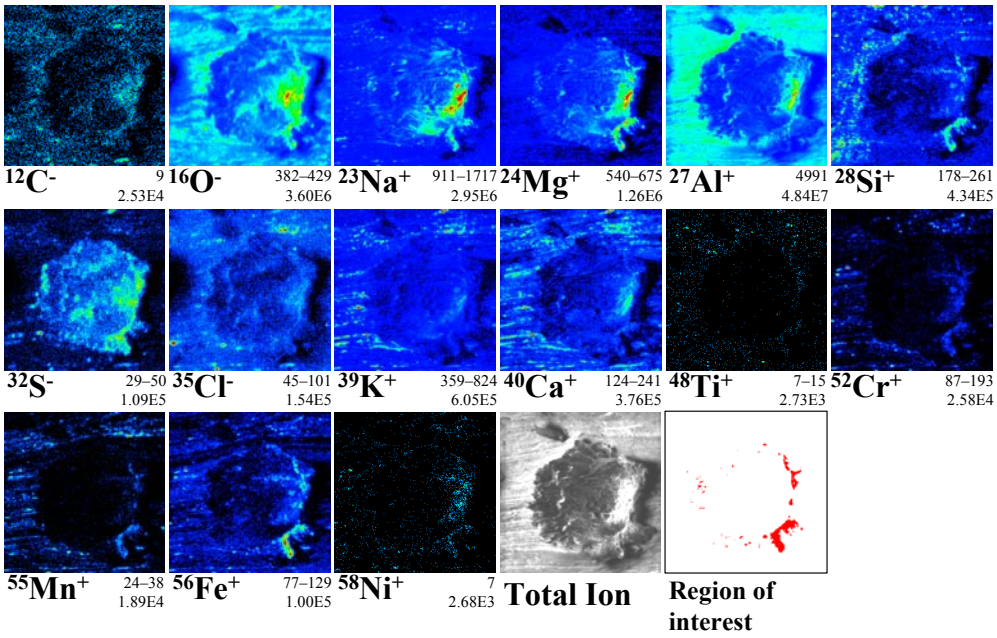

Fig. 13. Secondary ion images of the crater investigated on foil C2091N,1. The field of view is 98×98 μm^2.

C2102N,1

Two impact features were found on this foil; the first is a crater with a diameter of ~85 μm, the second is a multiple impact feature, most likely caused by an aggregate impactor.

Crater #1. A large area of residue is located in the "southeastern" area of the crater, while another patch of material is located in the upper left part of the rim (Fig. 14).

The main residue has abundant O, Na, Mg,Si, S, Cl, K, and Ca, and lower concentrations of B, C, Cr, Mn, Fe, and Ni, while the residual spot at the upper left contains mainly C, O, Si, Ca, and Fe.

Mg, Ca, Cr and Mn have roughly solar abundances (Fig. 16), while Fe and Ni are depleted by factors of 10 and 3, respectively, in comparison to CI abundances. The alkali elements Li, Na, and K are ~3–10×CI. The B, C and O contents of the crater residues cannot be determined unambiguously, due to the heterogeneous distribution of these elements on the surrounding foil blank. Nevertheless, the ion images shown in Fig. 14 suggest that the residue material contains a finite amount of B and C above background. Additionally, S shows a strong presence in the main residue, although quantification for S is not possible, due to the lack of appropriate standards. The abundance pattern displayed in Fig. 16 is quite similar to bulk CI composition for the major constituents of the residue, so the cometary particle is most likely a mixture of different components.

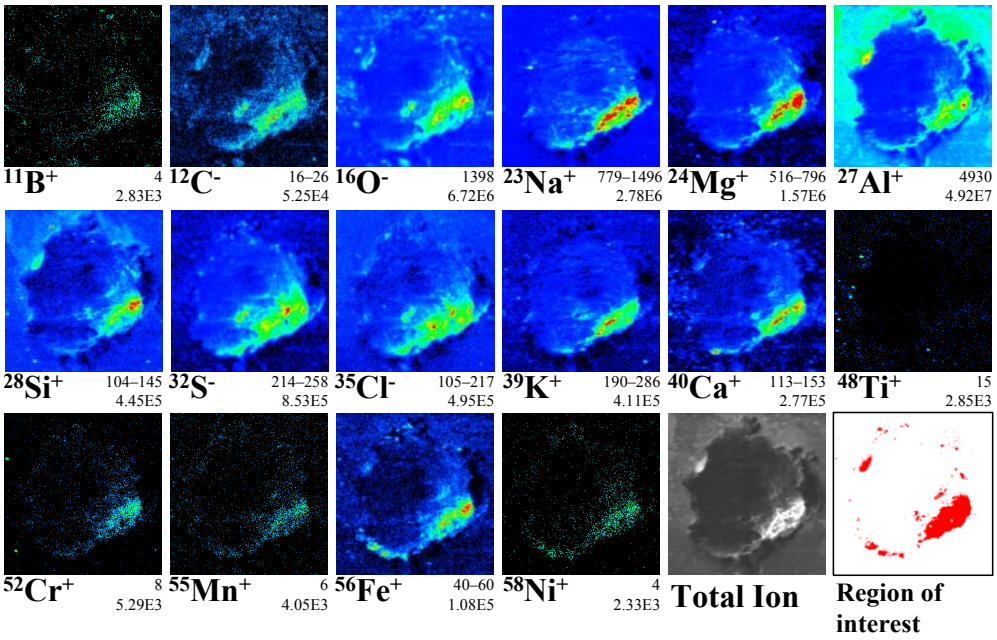

Fig. 14. Secondary ion images of crater #1 investigated on foil C2102N,1. The field of view is 115×118 μm^2.

Crater #2. The second impact feature has a much more complex distribution of elements, as can be seen in Fig. 15. There are high levels of Na, S, and Fe in the uppermost depression of the three major impact features. C, Mg, Si, Cr, and Mn are mainly located in the two lower craters, and Ca is quite evenly distributed in all three major depressions of this compound crater.

Overall, the bulk residue has a CI-like composition; the elements Li, Mg, Ca, Sc, Cr, Mn, Fe, Co, and Ni all are within 2×CI abundances. Only Na and K have high abundances of about 10×CI chondritic values (Fig. 16). The aggregate structure of the cometary projectile, together with most of the elements showing CI-like abundances suggests a rather polymict nature of the particle.

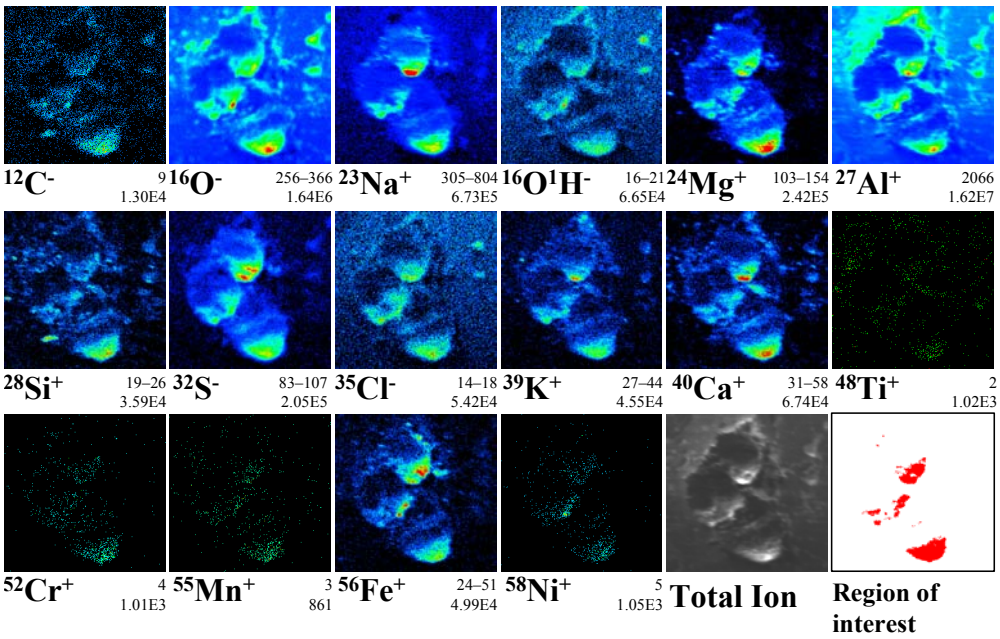

Fig. 15. Secondary ion images of crater #2 investigated on foil C2102N,1. The field of view is 55×56 μm^2.

Bulk element composition

In

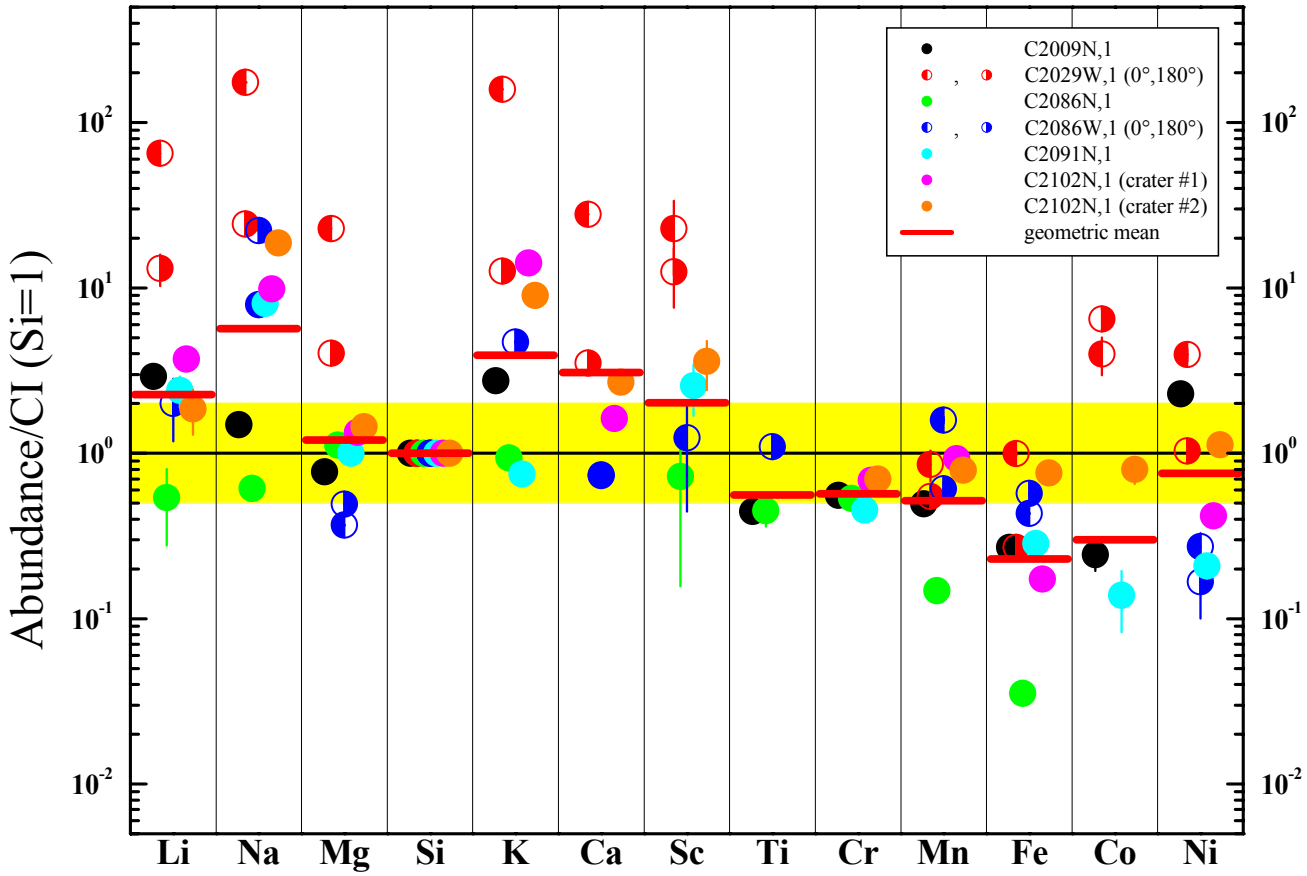

Fig. 16, element ratios relative to CI chondritic composition and normalized to Si for all seven analyzed impact residues are shown. The abundances of individual crater residues show a wide variation. This scattering is probably due to a monomineralic nature of several particles captured on the Al foils. No single mineral has a CI-like composition. Therefore, particles that show a good agreement with CI abundances must represent a mixture of different minerals.. But despite the rather large deviations of individual abundances from CI values, the geometric means of most element ratios are within 2×CI carbonaceous chondrite composition.

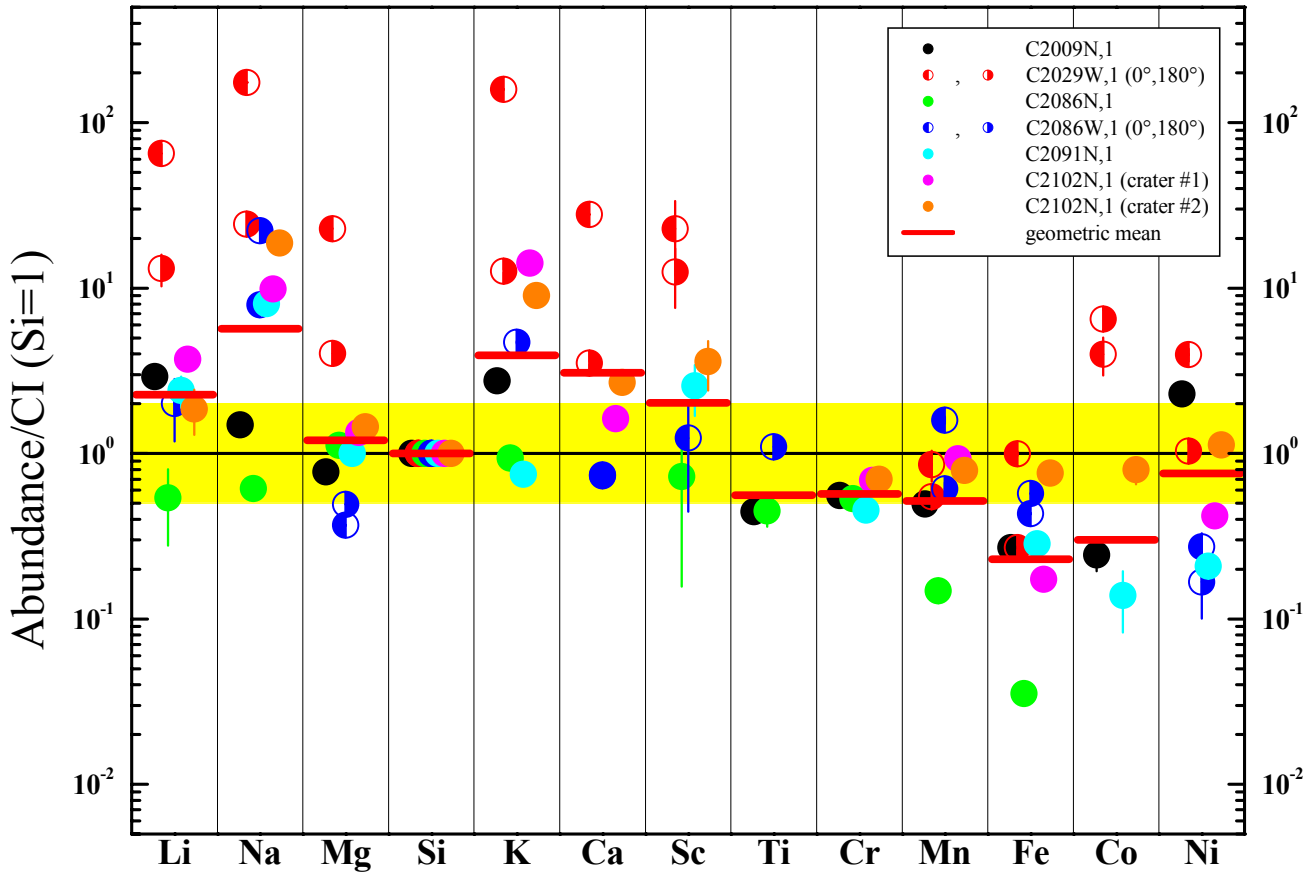

Fig. 16. Element ratios normalized to Si and CI for all seven crater residues analyzed. Data points between 0.5×CI and 2×CI abundances plot within the yellow area.

Table 1. Atomic element ratios relative to Si and corrected for Al foil blanks for the analyzed crater residues. Errors are given as last significant digit in parentheses.

	C2009N,1	C2029W,1 (0°)	C2029W,1 (180°)	C2086N,1	C2086W,1 (0°)	C2086W,1 (180°)	C2091N,1	C2102N,1 #1	C2102N,1 #2
Li	0.00017(2)	0.0037(5)	0.0008(2)	0.00003(2)		0.00011(5)	0.00014(3)	0.00021(1)	0.00011(3)
Na	0.0854(4)	10.04(2)	1.400(5)	0.0353(4)	0.456(1)	1.276(3)	0.463(1)	0.5469(5)	1.075(2)
Mg	0.829(2)	24.49(6)	4.31(2)	1.202(4)	0.393(3)	0.527(4)	1.069(3)	1.377(1)	1.552(4)
Si	1.00(1)	1.00(7)	1.00(4)	1.00(2)	1.00(2)	1.00(1)	1.00(1)	1.00(1)	1.00(2)
K	0.0104(1)	0.601(4)	0.048(1)	0.0035(1)		0.0177(4)		0.0512(1)	0.0339(3)
Ca		1.71(1)	0.215(3)		0.0453(8)	0.0448(8)		0.0957(3)	0.164(1)
Sc		0.0008(4)	0.0004(2)	0.00003(2)	0.00004(3)		0.00009(3)		0.00012(4)
Ti	0.0011(1)			0.0011(2)		0.0026(4)			
Cr	0.0075(2)			0.0072(3)		0.0012(3)	0.0061(4)	0.0062(1)	0.0094(4)
Mn	0.0047(2)	0.008(2)	0.0052(8)	0.0014(2)	0.0152(7)	0.0058(6)		0.0043(1)	0.0075(4)
Fe	0.24(1)	0.90(3)	0.24(1)	0.032(1)	0.389(4)	0.516(7)	0.26(2)	0.176(2)	0.68(3)
Co	0.0006(1)	0.009(2)	0.015(2)				0.0003(1)		
Ni	0.113(3)	0.19(2)	0.051(6)	0.0008(5)	0.013(3)	0.008(3)	0.010(2)	0.014(1)	0.055(5)

Organic material

Traces of complex organic matter, so-called polycyclic aromatic hydrocarbons (PAHs), which are present in primitive meteorites and interplanetary dust particles (IDPs) (Allamandola et al. 1987; Clemett et al. 1993; Messenger et al. 1998), were also found in six

of the seven analyzed residues (Fig. 17). Since PAHs are nearly omnipresent in nature (Allamandola 1996), it was not initially clear if the observed molecules are indigenous to the residual matter or terrestrial contaminants.

The craters on foils C2029W,1 and C2086N,1 show only very low sum intensities for PAHs in the mass range from 115 u to 302 u, and the PAH signal from the surrounding foil blank is about equal in intensity. It is therefore likely that these PAHs are largely contamination, and the following discussion will focus on only those crater residues with reasonably high PAH intensities above background.

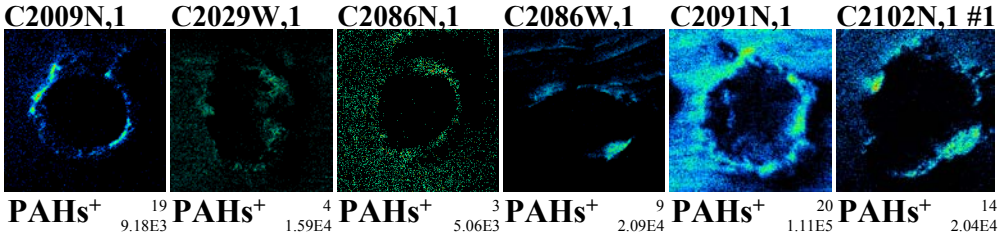

Fig. 17. Secondary ion images showing sum intensities of PAHs found in 6 crater residues. All secondary ion intensities for typical PAH masses between 115 u and 302 u are added.

In Fig. 18, a typical TOF-SIMS mass spectrum is shown. Displayed is the mass range that contains the dominant peaks of PAHs and PAH-fragments in the cometary crater residues.

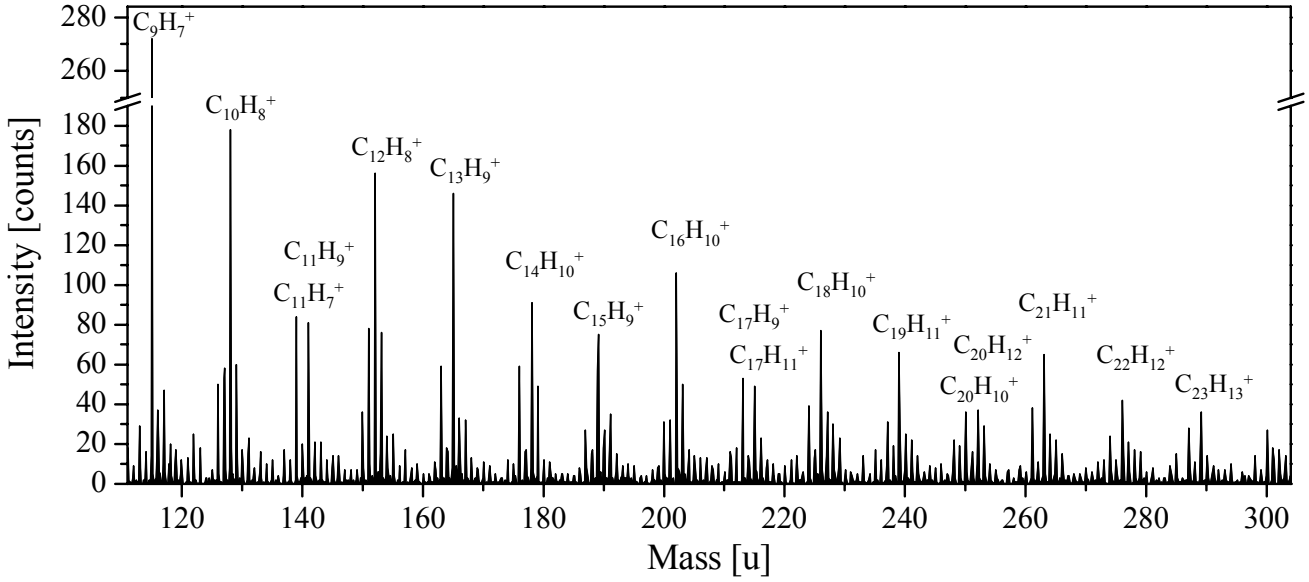

Fig. 18. Part of a TOF-SIMS mass spectrum of the crater residue C2009N,1 with sum formulae given for the major peaks. Relative maxima display typically mass differences of 11 or 13 u. In addition, there are often, several peaks present that are separated by a mass difference corresponding to the mass of H_2.

Fig. 19 shows the relative abundances of different PAHs with varying number of C atoms found in the secondary ion spectra of these craters. For comparison, the relative abundances of material from the meteorite Orgueil as well as residual matter from an Allende projectile shot onto Al foil at 6.1 km/s are displayed (Stephan et al. 2005, Hoppe et al. 2006). The PAHs in the analyzed crater residues on the foils C2009N,1, C2086W,1 and C2091N,1 show a much less steep decrease in abundance with increasing number of carbon atoms than other extraterrestrial samples like the carbonaceous chondrites Murchison and Orgueil (Stephan et al. 2003; Sandford et al. 2006). Even PAHs in the crater residue of the Allende test shot do

not show an abundance pattern similar to the cometary crater residues. The residual matter of crater #1 on C2102N,1, in contrast, shows a steep decrease comparable to that of Orgueil.

Although C2091N,1 has a comparably strong background signal of PAHs (see Fig. 17), the pattern of abundances displayed in Fig. 19 is very similar to the patterns of C2086W,1 and C2091N,1, which have no significant abundance of PAHs outside the crater residue.

Generally, the decrease of PAHs with increasing carbon number is less pronounced (Fig. 19) than it is for terrestrial samples and even for PAHs from primitive meteorites (Stephan et al. 2003). Thus, the cometary residues contain proportionally more 'heavier' PAH molecules than other extraterrestrial and terrestrial samples investigated so far.

Since complex molecules are easily fragmented and destroyed during the necessary sputter cleaning process, all data for the PAHs were obtained from TOF-SIMS analyses performed prior to sputter cleaning.

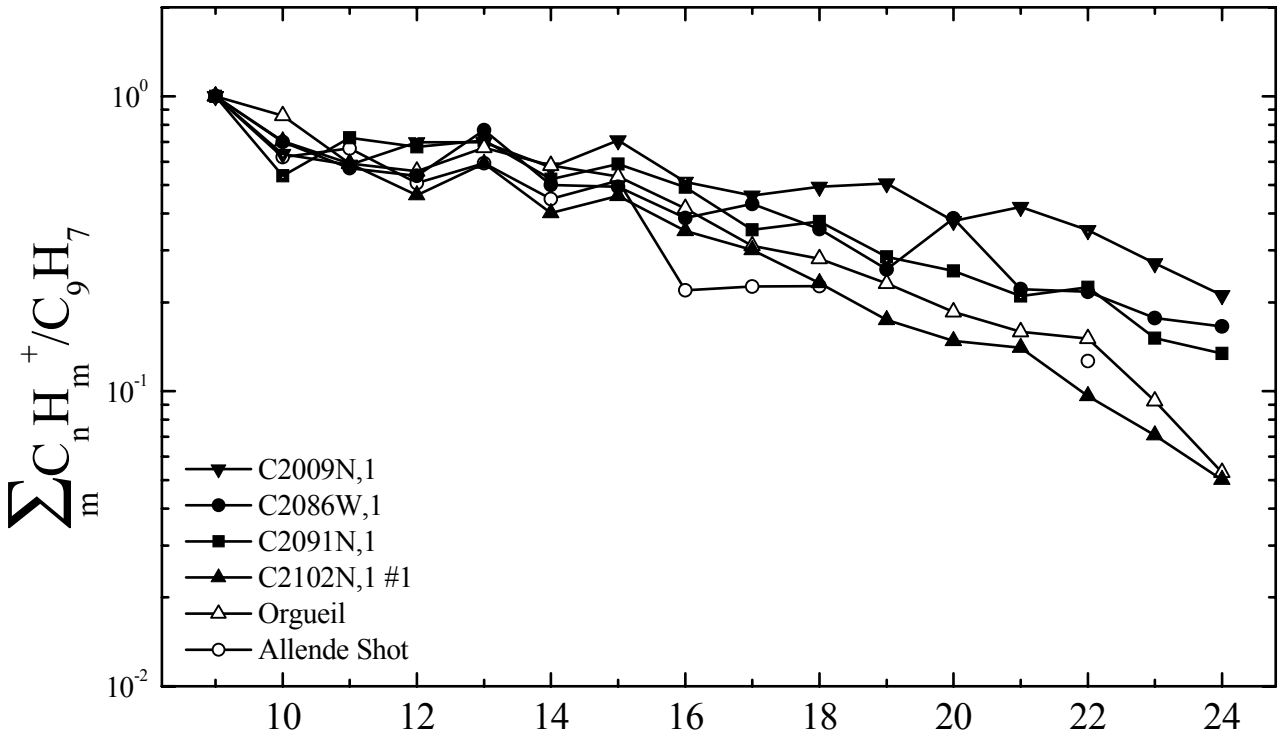

Fig. 19. Comparison of PAH signal intensities from four crater residues as discussed in the text with data from the CI carbonaceous chondrite Orgueil and material from an Allende test shot. The diagram shows the relative intensities of PAHs as a function of the number of carbon atoms relative to the intensity of $C_9H_7^+$.

DISCUSSION

Foils without large craters – C2026N,1, C2070W,1, and C2101W,1

The Si-features with associated hydrocarbons are most likely fine-grained aerogel debris that clings to the aluminum foils (

Fig. 4, Fig. 5 and Fig. 6). Aerogel pieces of different sizes located on the Al foils were clearly identifiable under the optical microscope, and features equivalent to those displayed in Fig. 5a and Fig. 5b were seen in the aerogel-contaminated foil areas. The Si-rich features found there contain (besides Si) C and O as main constituents (Fig. 5, Fig. 6 and Fig. 8), which is consistent with pre-flight analyses of the silica aerogel (Sandford et al. 2006). Consequently, these features were identified as aerogel debris.

The origin of the hot spots displaying correlated Mg- and Si-abundances is unknown; but their non-chondritic composition suggests that they are some kind of contamination (Fig. 7). Since these spots also contain C and O, as can be seen in Fig. 7, they are possibly processed, perhaps melted, aerogel that was relocated on the aluminum foils after particle impacts in the neighboring aerogel tiles. On the other hand, it presently cannot be excluded that they are a metallurgical contaminant of the Al foils, as are other elemental hotspots, containing Cr, Mn, Fe, Ni, Cu, Ba, and Tl. These are presumably impurities inherent in the foils, since they are not connected to crater-like structures. Furthermore, similar features occurred on the Al-1100-foils used in laboratory experiments (Hoppe et al. 2006; Leitner et al. 2006a; 2006b). Therefore, an extraterrestrial origin of these contaminants can be excluded.
The origin of the Tl-content of the spot shown in

Fig. 4b is not clear so far. Tl atoms can substitute alkali atoms like Na or K in compounds, since they have similar chemical properties, so it cannot be deduced if this Tl-spot is a metallurgical impurity indigenous to the Al foil, or if it is part of one of the observed alkali-containing surface contaminants.

Foil craters

The impact residues investigated on the foils exhibit, at a first glance, a wide range of element abundances. This is probably due to the fact that not only polymict particles were captured on the aluminum foils, but also compounds of few minerals or even nearly monomineralic grains that cannot show CI-like compositions, since no mineral with CI chondritic element abundances exists. This explains the wide scatter of abundances relative to Si and bulk CI composition observed in the crater residues.

In addition, the observed high abundances of some elements relative to Si and bulk CI values may be due to the effect already observed during the analysis of mineral standards. There, higher abundances than predicted from literature data and reference SEM-EDX analyses were observed especially for relatively volatile species like Na and K, but only where these elements are minor constituents or even trace elements in the analyzed materials (**Error! Reference source not found.**). I. e., the mobilization seems predominately to affect volatile elements with low initial relative abundances.

When considering the mineralogy of the residual matter in the investigated impact craters, there are two different groups of particles apparent on the foils. The first group consists of particles, that are nearly monomineralic or contain few distinct minerals, and so show quite wide deviations from bulk CI chondritic abundances (Fig. 16).

The largest scattering of data points is observed for the aggregate crater C2029W,1 that has a clearly non-silicate and FeS-containing composition (Fig. 10 and Table 1).

The particles creating the circular-shaped craters C2009N,1 and C2091N,1 show similar abundance patterns that may indicate a largely pyroxene-like nature, with virtually no Ca and a (Mg+Fe)/Si-ratio of ~1. The high abundances of Ni and Cu in a part of the crater rim of C2009N,1 are most likely caused by a Ni- and Cu-rich impurity indigenous to the foil. Evidence for such impurities was also found on foil C2070W,1 (see section above), without any correlation to an existing crater (Fig. 5d).

Furthermore, the Ni/Cu-ratio of the hotspots found on foil C2070W,1 (Fig. 5d) matches with the ratio determined for the rim area of the crater on C2009N,1 (~2.9 in both cases). Thus, it seems likely that a cometary particle creating the crater has hit one of the Ni-Cu-impurities in the foils and has mixed with it partially while creating the crater.

C2086N,1 is possibly another example for a monomineralic particle, since Mn and especially Fe are strongly depleted in comparison with bulk CI chondritic values. The Mg/Si-ratio of 1.2, together with the absence of Ca and the very low Fe abundance (Table 1) indicates a composition similar to enstatite.

The second group contains those cometary particles, that display a composition quite similar to CI chondrites and which therefore are polymict compounds of different mineral phases. The residues of C2102N,1 #2 C2086W clearly are of this type; their major constituents are well in the range of bulk CI composition. C2102N,1 #1 has an Fe/Si-ratio that is more similar to those observed for C2009N,1 and C2091N,1, but since this residue also has a CI-like Ca/Si-ratio, it seems to have a more complex composition than the two pyroxene-like particles, and therefore is more likely to be classified as polymict.

Organics

The seven investigated crater residues show a wide range of abundances of organic molecules. Apart from crater #2 on foil C2102N,1 which contained no complex organics at all, the six other residual craters have a PAH-bearing component. The origin and nature of these PAHs is not clear; terrestrial contamination has to be taken into account, but there are several indications for a non-terrestrial origin of the observed PAHs.

Especially the craters C2009N,1 and C2086W,1 show no significant abundance of PAHs in the neighborhood of their residues, making contamination of all crater areas with terrestrial organic matter unlikely. Furthermore, the very origin of the PAHs surrounding crater C2091N,1 is unknown; from their lateral distribution, it cannot be inferred if they are terrestrial contaminations or cometary matter deposited around the actual crater. So, a cometary origin of these PAHs cannot *a priori* be excluded.

Obviously, there exists a significant difference between the cometary organics and other primitive complex organic material, since the cometary residues contain proportionally more high-mass PAH molecules. This ‘enrichment’ in heavy PAHs is either simply due to organic material containing more heavy PAHs than were observed in other analyses, or it is caused by the preferential loss of low mass PAHs during impact on the foils (Stephan et al. 2003, Sandford et al. 2006). However, the latter explanation fails since during the Allende test shots a steeper decrease of PAH intensity with increasing mass was observed.

Additionally, the results from the analysis of crater #1 on C2102N,1 indicate the existence of another component of PAH-bearing material. This residue is obviously less ‘enriched’ in heavier PAHs and thus, looks similar to PAHs found in primitive meteorites like Orgueil. If this comparably lower content of heavy PAHs is indigenuous to the organic matter of the residue is still under discussion.

CONCLUSIONS

This study clearly demonstrates that TOF-SIMS is suitable for the identification and analysis of cometary impact residues captured in aluminum foil. Moreover, since TOF-SIMS is virtually non-destructive, the samples are still available for other analytical techniques after TOF-SIMS investigation.

The determination of the elemental compositions of the seven investigated foil crater residues was complicated by impurities intrinsic to the Al-foil targets used on Stardust, as well as surface contaminations. Nevertheless, unambiguous identification and analysis of all investigated residues was possible.

The cometary matter in the impact craters displays wide compositional span; nearly monomineralic grains, aggregates of non-silicate composition, as well as compact and aggregate particles of polymict compound were observed.

Furthermore, minor elements show a wide variety of elemental ratios throughout the samples, so they seem to be quite heterogeneously distributed in the cometary material. This is consistent with observations made for primitive meteorites (Brownlee et al. 1984). However,

the average element composition of the seven analyzed cometary residues is quite similar to bulk CI-chondritic values.

Furthermore, complex organic molecules like PAHs are present in most cometary particles captured on Stardust aluminum foil. The larger fraction of these PAH-bearing materials is richer in heavier PAHs relative to $C_9H_7^+$ than other extraterrestrial and also terrestrial samples. This is either due to a higher abundance of heavy PAHs in the cometary particles, or to preferential fractionation of low-mass molecules during the impact.

A smaller fraction of the PAH-bearing material does not display this relative high abundances in heavier PAH-components and resembles material from primitive meteorites or even terrestrial material. This similarity is either indigenous to the organic matter of the particle or an indicator for structural differences of the PAHs contained in the impactor and thus a different fragmentation behavior during the impact.

The TOF-SIMS investigation of elements as well as of organic compounds in the investigated crater residues reveals a quite heterogeneous composition of cometary matter.

Acknowledgements–We thank F. J. Stadermann for straightening the aluminum foils prior to our analysis. This work was supported by the *Deutsche Forschungsgemeinschaft* through grant STE 576/17-1. The Stardust mission to Comet 81P/Wild 2 was sponsored by NASA and executed jointly by the Jet Propulsion Laboratory and Lockheed Martin Space Systems. We are greatly indebted to many individuals who assured a successful comet encounter and who safely returned to Earth the Stardust collectors and its samples.

REFERENCES

Allamandola L. J. 1996. PAHs, they're everywhere! In *The Cosmic Dust Connection*, edited by Greenberg J. M. Dordrecht: Kluwer Academic Publishers. pp. 81–102.

Allamandola L. J., Sandford S. A., and Wopenka B. 1987. Interstellar polycyclic aromatic hydrocarbons and carbons in interplanetary dust particles and meteorites. *Science* 237:56–59.

Brownlee D. E., Tsou P., Anderson J. D., Hanner M. S., Newburn R. L., Sekanina Z., Clark B. C., Hörz F., Zolensky M. E., Kissel J., McDonnell J. A. M., Sandford S. A., and Tuzzolino A. J. 2003. Stardust: Comet and interstellar dust sample return mission. *Journal of Geophysical Research* 108:E8111.

Brownlee D. E., Wheelock M. M., and Bradley J. P. 1984. Point count analysis of interplanetary dust and fine-grained meteoritic materials (abstract). *Lunar Planet. Sci.* 15:94–95.

Clemett S. J., Maechling C. R., Zare R. N., Swan P. D., and Walker R. M. 1993. Identification of complex aromatic molecules in individual interplanetary dust particles. *Science* 262:721–725.

Hoppe P., Stadermann F. J., Stephan T., Floss C., Leitner J., Marhas K. K., and Hörz F. 2006. SIMS studies of Allende projectiles fired into Stardust-type aluminum foils at 6 km/sec. *Meteoritics & Planetary Science* 41:197–209.

Hörz F., Fechtig H., Janicke J., and Schneider E. 1983. Morphology and chemistry of projectile residue in small experimental impact craters. *Journal of Geophysical Research* 88:B353–B363.

Leitner J., Stephan T., and Hörz F. 2006a. TOF-SIMS analysis of residues of projectiles shot onto Stardust aluminum foil (abstract). *Lunar Planet. Sci.* 37:#1576.

Leitner J., Stephan T., Kearsley A. T., and Hörz F. 2006b. TOF-SIMS analysis of crater residues from projectiles shot onto aluminum foil (abstract). *Meteoritics & Planetary Science* 41:A105.

Messenger S., Amari S., Gao X., Walker R. M., Clemett S. J., Chillier X. D. F., Zare R. N., and Lewis R. S. 1998. Indigenous polycyclic aromatic hydrocarbons in circumstellar graphite grains from primitive meteorites. *Astrophysical Journal* 502:284–295.

Rost D., Stephan T., and Jessberger E. K. 1999. Surface analysis of stratospheric dust particles. *Meteoritics & Planetary Science* 34:637–646.

Sandford S. A., Aléon J., Alexander C. M. O., Araki T., Bajt S., Baratta G. A., Borg J., Bradley J. P., Brownlee D. E., Brucato J. R., Burchell M. J., Busemann H., Butterworth A., Clemett S. J., Cody G., Colangeli L., Cooper G., d'Hendecourt L., Djouadi Z., Dworkin J. P., Ferrini G., Fleckenstein H., Flynn G. J., Franchi I. A., Fries M., Gilles M. K., Glavin D. P., Gounelle M., Grossemy F., Jacobsen C., Keller L. P., Kilcoyne A. L. D., Leitner J., Matrajt G., Meibom A., Mennella V., Mostefaoui S., Nittler L. R., Palumbo M. E., Papanastassiou D. A., Robert F., Rotundi A., Snead C. J., Spencer M. K., Stadermann F. J., Steele A., Stephan T., Tsou P., Tyliszczak T., Westphal A. J., Wirick S., Wopenka B., Yabuta H., Zare R. N., and Zolensky M. E. 2006. Organics captured from comet Wild 2 by the Stardust spacecraft. *Science*:in press.

Stadermann F. J., Hoppe P., Floss C., Heck P., Huth J., Kearsley A. T., Leitner J., Stephan T., Hörz F., and McKeegan K. D. 2006. Stardust in STARDUST – the C, N, and O isotopic compositions of Wild 2 cometary residues in Al foil impacts (abstract). *Meteoritics & Planetary Science*:in prep.

Stephan T. 2001. TOF-SIMS in cosmochemistry. *Planetary and Space Science* 49:859–906.

Stephan T., Jessberger E. K., Heiss C. H., and Rost D. 2003. TOF-SIMS analysis of polycyclic aromatic hydrocarbons in Allan Hills 84001. *Meteoritics & Planetary Science* 38:109–116.

Stephan T., Leitner J., and Hörz F. 2005. TOF-SIMS analysis of residues from Allende projectiles shot onto aluminum foil – a Stardust dress rehearsal. In *Workshop on Dust in Planetary Systems* LPI Contribution No. 1280, Houston: Lunar and Planetary Institute. pp. 136–137.

Tsou P., Brownlee D. E., Sandford S. A., Hörz F., and Zolensky M. E. 2003. Wild 2 and interstellar sample collection and Earth return. *Journal of Geophysical Research* 108:E8113.